Ann. Geophys., 26, 3933–3943, 2008
www.ann-geophys.net/26/3933/2008/

Annales Geophysicae

Wavelength dependence of the E_s layer instability, and of coupling to the F layer, in the nonlinear regime

R. B. Cosgrove

Center for Geospace Studies, SRI International, Menlo Park, CA, USA

Received: 14 May 2008 – Revised: 27 September 2008 – Accepted: 29 October 2008 – Published: 5 December 2008

Abstract. The E_s layer instability has been suggested as a participant in the creation of frontal structures observed in both the E_s and F layers of the nighttime midlatitude ionosphere, in spite of the fact that the spatial scales of the frontal structures are very different in the two layers. The linear growth rate of the instability has a maxima in the vicinity of the wavelength observed for the E_s layer structures (short wavelengths). However, the maxima is non-distinct, and simulations have shown that the instability is extremely nonlinear. Therefore, to understand the wavelength dependence of the E_s layer instability it is necessary to factor in nonlinear behavior. Simulations have shown that the instability is active at the wavelengths observed in the F layer, and revealed that the E_s layer behavior at these long wavelengths is so nonlinear that the common, highly localized E_s layer observation techniques would likely miss the signature, which is highly visible in the F layer. However, there is currently no explanation for why long wavelengths so clearly dominate short (or intermediate) wavelengths in the F layer observations, and this is a weakness in arguments that the E_s layer instability participates in the creation of F-region frontal structures. Herein we remove this weakness by showing that longer wavelengths grow to larger amplitudes before eventual nonlinear saturation, and couple more effectively to the F-region.

Keywords. Ionosphere (Mid-latitude ionosphere; Modeling and forecasting; Plasma waves and instabilities)

1 Introduction

Cosgrove and Tsunoda (2002) showed that the equilibrium configuration of a midlatitude sporadic-E (E_s) layer at a wind shear node is unstable, at night, to plane wave perturbations in altitude or field-line-integrated (FLI) density. This instability is a possible participant in frontal structuring events in E_s layers, and in the F layer, which have been observed over the years by ionosonde, by coherent scatter radar, by all-sky images of 630.0 nm emissions, and by GPS time delay mapping (Tsunoda and Cosgrove, 2001; Tsunoda et al., 2004). Participation of the E_s layer instability is suggested by the fact that the observed structures prefer the same skewed azimuthal alignment that maximizes the instabilities growth rate. The general correlation between the type of coherent radar backscatter from E_s layers known as quasi-periodic (QP) echoes (Yamamoto et al., 1991), and the F-region frontal disturbances known as mesoscale traveling ionospheric disturbances (MSTIDs) has been asserted by Saito et al. (2007). A specific example of correlation between the airglow intensity and the E_s layer electric fields has been documented by Otsuka et al. (2007). The instability is also potentially involved in the source of large polarization electric fields in E_s layers, and in the F layer, which have been indicated by incoherent scatter radar (Behnke, 1979), by coherent scatter radar (e.g. Schlegel and Haldoupis, 1994; Tsunoda et al., 1994; Fukao et al., 1991), and measured in situ during the two SEEK rocket campaigns (Fukao et al., 1998; Pfaff et al., 1998; Yamamoto et al., 2005; Pfaff et al., 2005). We explore in this work the stark contrast between the wavelengths of structure observed in the E_s and F layers, with respect to a possible E_s layer electrodynamic contribution to the source, by investigating the wavelength dependence of the E_s layer instability in the nonlinear regime.

Spaced ionosonde observations (Goodwin and Summers, 1970) have revealed the consistent presence of frontal structures in Southern Hemisphere E_s layers, with fronts elongated from northeast to southwest. Tsunoda et al. (2004) noted that this orientation points to the E_s layer instability as source. Goodwin and Summers (1970) found that the (horizontal) wavelength range for the frontal structures was 10–40 km, with a mean of 24 km.

Correspondence to: R. B. Cosgrove
(russell.cosgrove@sri.com)

Published by Copernicus Publications on behalf of the European Geosciences Union.

QP echoes have been found to form frontal structures with a preferred orientation matching that of the E_s layer instability (Yamamoto et al., 1994, 1997; Hysell et al., 2004; Larsen et al., 2007; Saito et al., 2007). This orientation, observed in the Northern Hemisphere, is conjugate along magnetic field lines to that observed in the Southern Hemisphere by Goodwin and Summers (1970). Such conjugacy is a basic feature of the E_s layer instability. By examining profiles of QP echo Doppler velocity presented by various authors, a wavelength in the perpendicular to $\boldsymbol{B}$ direction can be inferred. This was done in Cosgrove (2007b), where a wavelength range of 8–24 km, with a mean of 17 km, was found. Hence, the estimated wavelength for QP echoes is slightly, but not significantly less than the estimated wavelength for ionosonde observed frontal structures.

In contrast, much longer wavelength structures have been observed in the F-region, which also share the same preferred orientation. All sky images (e.g. Garcia et al., 2000; Kubota et al., 2001; Saito et al., 2001; Shiokawa et al., 2003) and GPS time delay (e.g. Saito et al., 1998; Tsugawa et al., 2007) show nighttime F layer structure with a clear statistical tendency to form fronts elongated from northwest to southeast (Northern Hemisphere), and generally propagating to the southwest. We will refer to these observations as medium traveling ionospheric disturbances (MSTIDs). The wavelength for MSTIDs ranges from 50 km to 300 km, with a preference for about 200 km (Garcia et al., 2000; Shiokawa et al., 2003). These scales seem consistent with the idea that E_s layers may be involved in the source mechanism. Cathey (1969) categorized E_s layer sizes with a satellite born ionospheric sounder, finding a mean of 170 km, and a maximum of 1000 km. Goodwin (1966) found E_s layer fronts extending 1000 km, by correlating the backscatter from spaced ionosondes.

The observed 8–40 km wavelengths for E_s layer structure are nearly an order of magnitude below the 50–300 km wavelengths observed in the F layer. Nevertheless, simulations by Cosgrove and Tsunoda (2003), and Cosgrove (2007a), have shown that the E_s layer instability is a potential contributor to both the smaller scale E_s layer structure, and the larger scale F layer structure. The simulations in Cosgrove (2007a) found that when the E_s layer instability was seeded at long wavelengths, the resulting E_s layer evolution was so highly nonlinear that it would be almost impossible for E-region observing apparatus to connect it with a long wavelength event. There is not, for example, a 10 km sinusoidal modulation of the E_s layer altitude with a 200 km wavelength. On the other hand, the associated F layer structure in the simulations clearly reflects the long wavelength. Hence, the simulations seem thus far to be consistent with the observations. However, one question that remains unaddressed is, if the E_s layer instability is active at both long and short wavelengths, why are there predominantly long wavelength structures in the F layer?

Cosgrove (2006b) found through a linear growth rate computation that the E_s layer instability is stabilized for wavelengths less than a few times the equilibrium layer thickness, and has a growth rate maxima slightly above the short wavelength cuttoff, due to the reduced mapping efficiency of E_s layer polarization electric fields to the F layer that occurs as wavelength is reduced. However, the growth rate maxima is not a strong one, and there is no reason to rule out excitation of the instability at long wavelengths, to the extent that the dimensions of the E_s layer are sufficiently large. Also, Cosgrove (2006a) found that the nonlinear aspects of the E_s layer electrodynamics are extremely important, and therefore must be factored into any analysis of the wavelength dependence of the E_s layer instability. We therefore undertake in this paper to address the wavelength dependence of the E_s layer instability in the nonlinear regime, and to see if the result sheds light on the preferred wavelength for the F layer frontal structure observations.

2 Larger saturation amplitude for longer wavelength

2.1 Theory

Consider time-dependent plasma density, ion velocity, and electron velocity distributions n, $\boldsymbol{v}_i$, and $\boldsymbol{v}_e$, respectively, which satisfy the equations of motion in the zonal wind shear field

$$\boldsymbol{u} = uz\hat{y}'', \tag{1}$$

where $\hat{y}''$ is eastward, z is a vertical coordinate (positive downward), x and y will be horizontal coordinates, and u is the constant zonal wind shear. By the equations of motion we mean the quasi-neutral ion and current continuity equations $\frac{\mathrm{d}n}{\mathrm{d}t}+\nabla\cdot(n\boldsymbol{v}_i)=0$ and $\nabla\cdot(n(\boldsymbol{v}_i-\boldsymbol{v}_e))=0$, where $\boldsymbol{v}_i$ and $\boldsymbol{v}_e$ are determined from the steady state momentum equations using the wind field (Eq. 1) and a polarization electric field $\boldsymbol{E}$. If the spatial scale of the density distribution is increased by a factor σ, then according to Eq. (1) the wind velocity at corresponding points is also increased by the factor σ, and the equations of motion will be satisfied by increasing the polarization electric fields by the same factor σ.

Specifically, consider the rescaled plasma density

$$n'(x, y, z) = \gamma n(x/\sigma, y/\sigma, z/\sigma), \tag{2}$$

and the rescaled ion and electron velocities

$$\boldsymbol{v}'_{i,e}(x, y, z) = \beta\boldsymbol{v}_{i,e}(x/\sigma, y/\sigma, z/\sigma), \tag{3}$$

where σ, γ, and β are constants. Plugging into the current continuity equation $\nabla\cdot(n(\boldsymbol{v}_i-\boldsymbol{v}_e))=0$ we find $\nabla\cdot(n'(\boldsymbol{v}'_i-\boldsymbol{v}'_e))=0$, that is, the rescaled triple $(n', \boldsymbol{v}'_i, \boldsymbol{v}'_e)$ also satisfies the current continuity equation. To check the ion continuity equation for the pair $(n', \boldsymbol{v}'_i)$ we compute the time

derivative of n', using the assumption that $(n, \boldsymbol{v}_i)$ satisfies the ion continuity equation:

$$\begin{aligned}\frac{\mathrm{d}}{\mathrm{d}t}n'(x, y, z) &= \frac{\mathrm{d}}{\mathrm{d}t}(\gamma n(x/\sigma, y/\sigma, z/\sigma)) \\ &= -\gamma\left[\nabla\cdot(n\boldsymbol{v}_i)\right]_{(x/\sigma, y/\sigma, z/\sigma)} \\ &= -\frac{\sigma}{\beta}\left[\nabla\cdot(n'\boldsymbol{v}_i')\right]_{(x,y,z)}. \end{aligned} \quad (4)$$

Equation (4) shows that the pair $(n', \boldsymbol{v}_i')$ satisfies the ion continuity equation when $\beta{=}\sigma$. Therefore, the equations of motion are satisfied by the rescaled quantities defined in Eqs. (2) and (3) if there is a polarization field $\boldsymbol{E}'$ such that $\boldsymbol{v}_i'$ and $\boldsymbol{v}_e'$ satisfy the steady state momentum equations with $\beta{=}\sigma$, using the wind field (Eq. 1).

According to the steady state momentum equations the ion and electron velocities are locally determined, and proportional to $\boldsymbol{u}$ and the electric field $\boldsymbol{E}$, that is,

$$\begin{aligned}&\text{if } \boldsymbol{u}(\boldsymbol{x}) \to \alpha\boldsymbol{u}(\boldsymbol{x}') \text{ and } \boldsymbol{E}(\boldsymbol{x}) \to \alpha\boldsymbol{E}(\boldsymbol{x}'), \\ &\quad\text{then } \boldsymbol{v}_{i,e}(\boldsymbol{x}) \to \alpha\boldsymbol{v}_{i,e}(\boldsymbol{x}'), \quad \text{for any } \alpha, \end{aligned} \quad (5)$$

where the notation $\to$ is used to mean "is replaced by." The wind field (Eq. 1) is self-similar in the sense $\boldsymbol{u}(x, y, z){=}\sigma\boldsymbol{u}(x/\sigma, y/\sigma, z/\sigma)$. Therefore, with the wind field (Eq. 1), and a rescaled electric field

$$\boldsymbol{E}'(x, y, z) = \sigma\boldsymbol{E}(x/\sigma, y/\sigma, z/\sigma), \quad (6)$$

the relation (5) gives the rescaled velocities $\boldsymbol{v}_{i,e}'$ in Eq. (3), with $\beta{=}\sigma$. This shows that the equations of motion are satisfied by the rescaled quantities

$$\begin{aligned}&n'(x, y, z) = \gamma n(x/\sigma, y/\sigma, z/\sigma), \quad \text{and} \\ &\boldsymbol{E}'(x, y, z) = \sigma\boldsymbol{E}(x/\sigma, y/\sigma, z/\sigma), \end{aligned} \quad (7)$$

for any constants σ and γ, using the wind field (Eq. 1). (Note that choosing $\gamma{=}1/\sigma$ preserves the FLI density under the transformation (2).)

This result holds exactly, for any n, and means that the density fields n and n' track each other exactly, with the rescaling factors σ and γ, no matter how nonlinear the evolution becomes. If, for example, $\sigma{=}2$, and n is an E_s layer with an initial sinusoidal perturbation of wavelength λ, then n' is an E_s layer with an initial sinusoidal perturbation of wavelength 2λ. The maximum polarization electric field associated with n' is double the maximum associated with n. Likewise, the maximum vertical scale associated with n' is double that associated with n, etc.

Therefore, we have in effect derived the power spectrum for the structure generated by the E_s layer instability (in simplest form), which might apply under an assumption akin to the concept of fully developed turbulence that arises in the theory of turbulent fluids. In this regard, the scaling operation also affects the amplitude of the initial sinusoidal perturbation. If the amplitude is not rescaled then the derivation above, specifically Eq. (4), is not valid. The interpretation that we have derived the power spectrum relies on an assumption that the final saturation amplitude is not sensitive to the initial perturbation amplitude, which is what we mean by "an assumption akin to the concept of fully developed turbulence." The simulations below will employ the same initial amplitude for all wavelengths, and hence will test this assumption.

When there is an F-region wind $\boldsymbol{u}_F$, and/or an unsheared meridional wind u_N in the E-region, then the additional scaling relations

$$\begin{aligned}&\boldsymbol{u}_F'(x, y, z) = \sigma\boldsymbol{u}_F(x/\sigma, y/\sigma, z/\sigma) \text{ and} \\ &u_N'(x, y, z) = \sigma u_N(x/\sigma, y/\sigma, z/\sigma) \end{aligned} \quad (8)$$

must be assumed for the above derivation to go through. This is an alteration of the background conditions. Hence, our results concerning the rescaling with wavelength of the maximum electric field, and of the maximum vertical scale, do not hold exactly under these more general conditions. We turn now to numerical simulations to verify that the results are at least qualitatively correct, that is, that the E_s layer instability creates larger electric fields and more vertical excursion of plasma at longer wavelengths.

2.2 Simulations

To investigate the wavelength dependence of the E_s layer instability with F-region and meridional E-region winds, we apply the simulation developed by Cosgrove (2006a). This is a two-dimensional numerical solution of the two-fluid equations, simultaneously covering the E_s and F layers, coupled by the assumption that the electric field maps perfectly along the magnetic field $\boldsymbol{B}$. The conditions are set up to match Fig. 5 of Cosgrove (2006a), with wavelengths of 200 km, 100 km, 50 km, and 25 km. By wavelength we mean the wavelength of the initial seed altitude perturbation, which is given in the F layer. The E_s layer is initially flat. The E_s layer is unstable to the E_s layer instability, the F layer is unstable to the Perkins instability (Perkins, 1973), and there is a relative horizontal velocity between the two layers of 120 m/s. The latter condition is what is referred to by Cosgrove and Tsunoda (2004) and Cosgrove (2006a) as the non-resonant condition. In this case, and if the E_s layer is sufficiently dense, Cosgrove (2006a) found that the role of the Perkins instability is mostly to seed the E_s layer instability, and that the interesting electrodynamics comes from the nonlinearity of the E_s layer instability. The "sufficiently dense" criteria was found numerically to be $\Sigma_H/\Sigma_{PF} \gtrsim 1$, where Σ_H is the FLI Hall conductivity of the E_s layer, and Σ_{PF} is the FLI Pedersen conductivity of the F layer.

Details of the simulation parameters are as follows: a rotational wind shear profile is used, with a sinusoidal variation of the zonal wind, and a co-sinusoidal variation of the meridional wind. At the equilibrium altitude of the E_s layer this gives a southward wind of 120 m/s, with a zonal windshear of 35 m/s/km (westward above and eastward below).

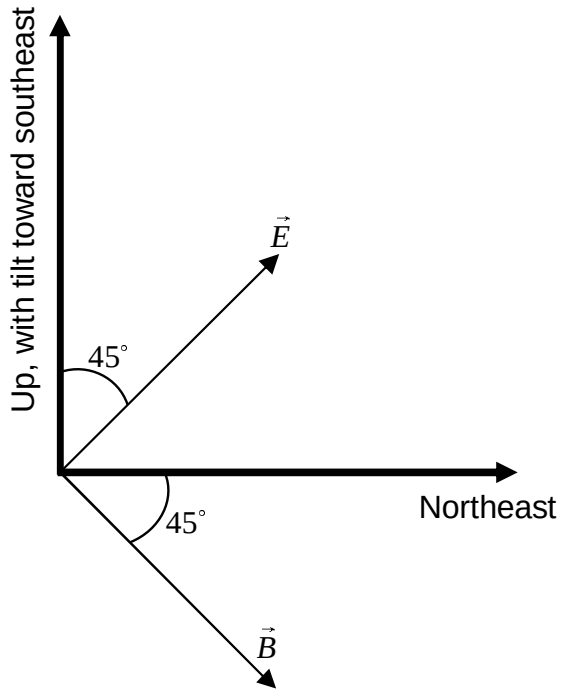

Fig. 1. Axis orientation for Figs. 2 through 5. The coordinate axes, $\boldsymbol{E}$, and $\boldsymbol{B}$, all lie in the planes of the figures.

A uniform wind field of 45 m/s to the east, and 22 m/s to the south, is applied in the F-region. There is no background (i.e. not caused by polarization of the E_s layer) electric field. A 0.6 km half width Gaussian density profile is located at the zonal wind shear node on the E-region grid, and a 120 km half width Gaussian density profile is located on the F-region grid. The ion-neutral collision frequency is computed from a curve fit to data given by Johnson (1961), with the E_s layer located at an altitude of 100 km. The ratio of the E_s layer FLI Hall conductivity to the F layer FLI Pedersen conductivity is set to $\frac{\Sigma_H}{\Sigma_{PF}}$=1.8. This leads to a ratio of E_s layer FLI Pedersen conductivity to F layer FLI Pedersen conductivity of $\frac{\Sigma_{PE}}{\Sigma_{PF}}$=0.06. Details of the simulation method may be found in Cosgrove (2006a).

The simulation results are presented in Figs. 2 through 5. The figures show cross sections of the E_s layer and F layer densities in grey scale, and the electric field at the equilibrium altitude of the E_s layer. The scales for all figures are in kilometers, except for the y-axis of the electric field figures, which is in mV/m. The orientation of the coordinate axes is summarized in Fig. 1. The axes are defined so that both $\boldsymbol{B}$ and $\boldsymbol{E}$ lie in the figure plane. The x-axis is northeast, and $\boldsymbol{B}$ makes a 45° angle with the x-axis, directed from top left to bottom right. The electric field $\boldsymbol{E}$ is perpendicular to $\boldsymbol{B}$, with positive defined from bottom left to top right. The sacrifice for making $\boldsymbol{B}$ and $\boldsymbol{E}$ lie in the plane of the figure is that the y-axis is directed upward, and a little toward the southeast. The x-axis, however, is exactly horizontal.

The time periods shown in Figs. 2 through 5 are chosen to bracket the wave-breaking events, which constitute the explosive growth phase of the instability. The maximum electric field occurs simultaneously with the wave-breaking event. Before the wave breaking event there is little visible activity in the layer, and the electric field is small. After the wave breaking event the electric field again decreases, and the layer structure becomes more disorganized. The shorter the wavelength of the initial seed modulation, the longer it takes for the wave-breaking event to occur.

Comparing the electric field plots in Figs. 2 through 5 confirms the finding that the maximum electric field (maximum occurring over the course of the evolution subsequent to the initial 5 km altitude modulation of the F layer) grows with wavelength. Figure 6 shows $\log_2$–$\log_2$ plots of the maximum electric field versus the wavelength of the initial modulation, as found by the simulations presented in Figs. 2 through 5, and by applying the scaling rule of Sect. 2.1 (theory). The horizontal axis of Fig. 6 is $\log_2$ of wavelength in km, and the vertical axis is $\log_2$ of maximum electric field in mV/m. The scaling rule is applied by setting the theoretical and simulated electric field maxima equal at λ=25 km ($\log_2(25)$=4.64), and scaling to the longer wavelengths. Figure 6 shows that the scaling rule works well for the first two doublings of the wavelength, but fails for the third.

The fact that the effect is less than a direct proportionality is consistent with the expectations developed in Sect. 2.1, where we noted that a direct proportionality would result only if the E_s layer meridional wind, and the F layer winds, were also rescaled.

An additional factor arises because the simulation employs a rotational wind shear, and hence does not have a strictly linear variation of the zonal wind with altitude. This may be responsible for the large deviation from linearity observed in Fig. 6 between λ=100 km and λ=200 km, because it is in this wavelength-range that the maximum altitude excursion of the E_s layer modulation (which increases with wavelength, along with the maximum electric field) approaches one-quarter of a wavelength of the rotational wind shear. The altitude-excursion approaches the end of the zonal-wind-shear region, as the approximation $\sin\varepsilon \simeq \varepsilon$ begins to break down. Also, the meridional wind, which is essential to the instability (Cosgrove, 2007b), is significantly decreased – as the altitude excursion moves away from the peak of the cosine.

With regard to the increase in F layer altitude displacement associated with increasing wavelength, we note that in addition to the fact that the E_s layer produced electric fields increase with wavelength, the interaction time between the two layers also increases with wavelength. Specifically, since the relative horizontal velocity (between the E_s and F layers) is fixed, a longer wavelength means that it takes longer for the electric field seen by a particular piece of F layer plasma to be reversed, due to relative drift. This longer interaction time,

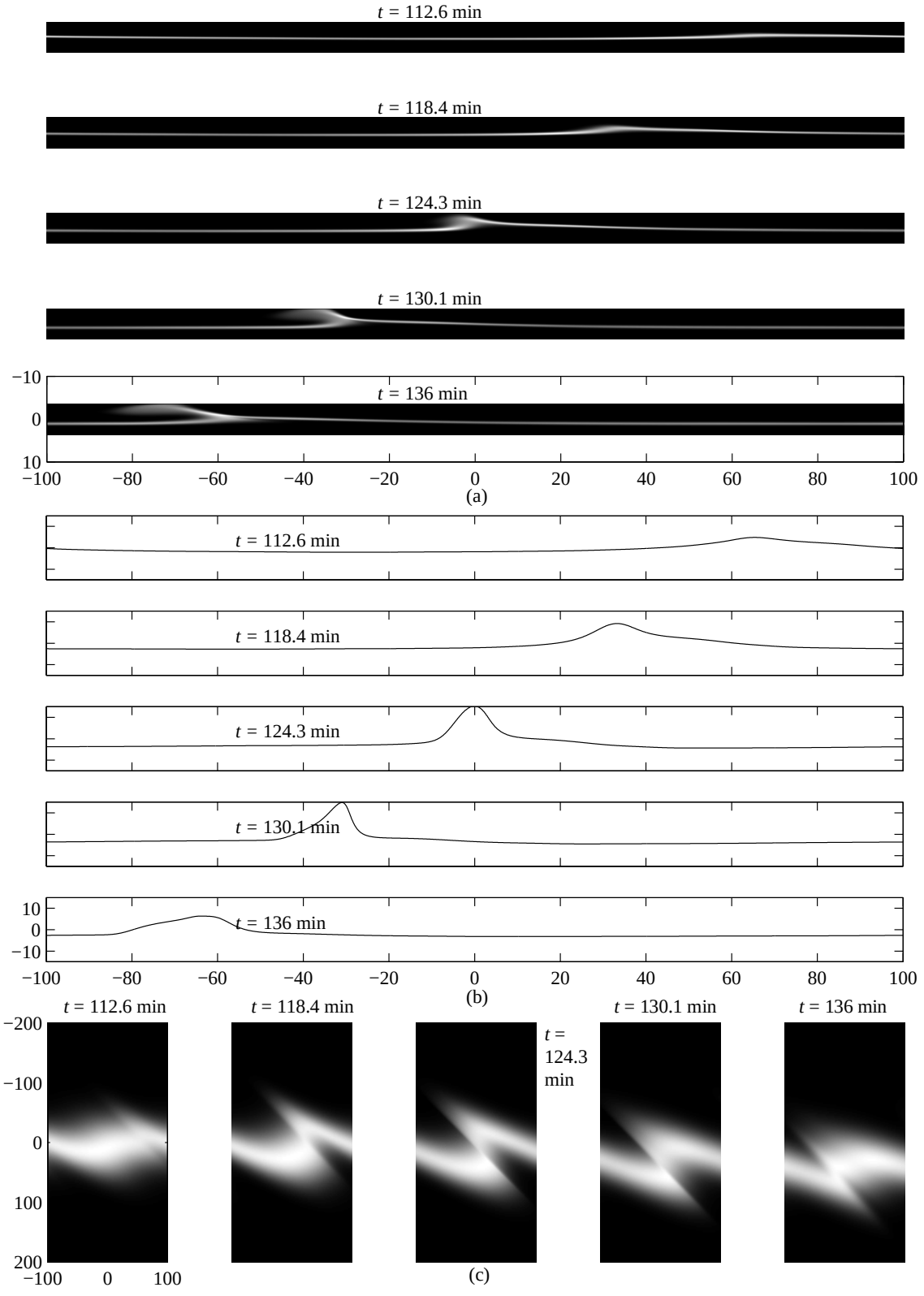

Fig. 2. Seed wavelength of 200 km with $\frac{\Sigma_H}{\Sigma_{PF}}$=1.8. **(a)** E_s layer, **(b)** electric field, and **(c)** F layer. The axes for all figures are described in Sect. 2.2, and summarized in Fig. 1.

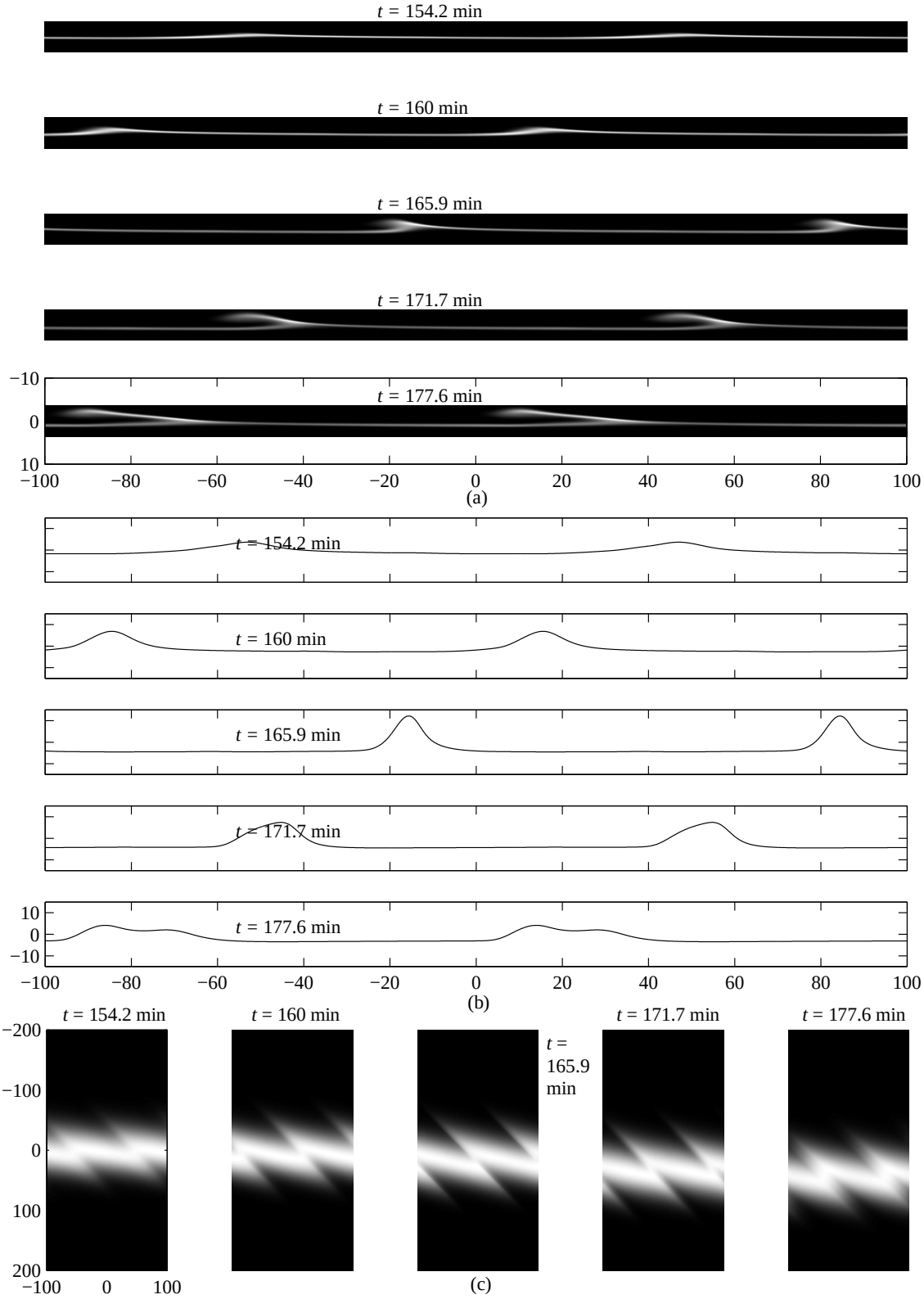

Fig. 3. Seed wavelength of 100 km with $\frac{\Sigma_H}{\Sigma_{PF}}$=1.8. **(a)** E_s layer, **(b)** electric field, and **(c)** F layer. The axes for all figures are described in Sect. 2.2, and summarized in Fig. 1.

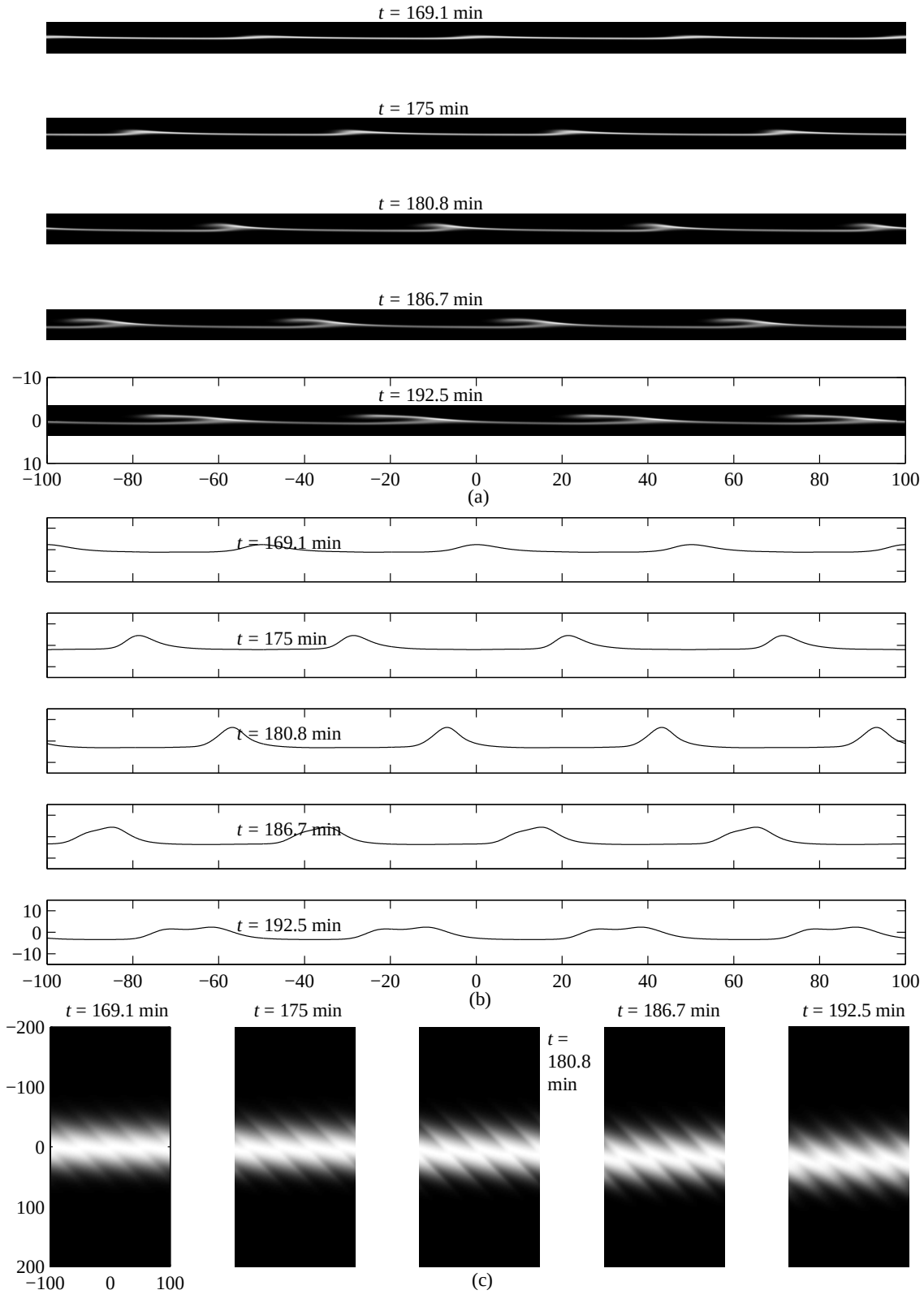

Fig. 4. Seed wavelength of 50 km with $\frac{\Sigma_H}{\Sigma_{PF}}$=1.8. **(a)** E_s layer, **(b)** electric field, and **(c)** F layer. The axes for all figures are described in Sect. 2.2, and summarized in Fig. 1.

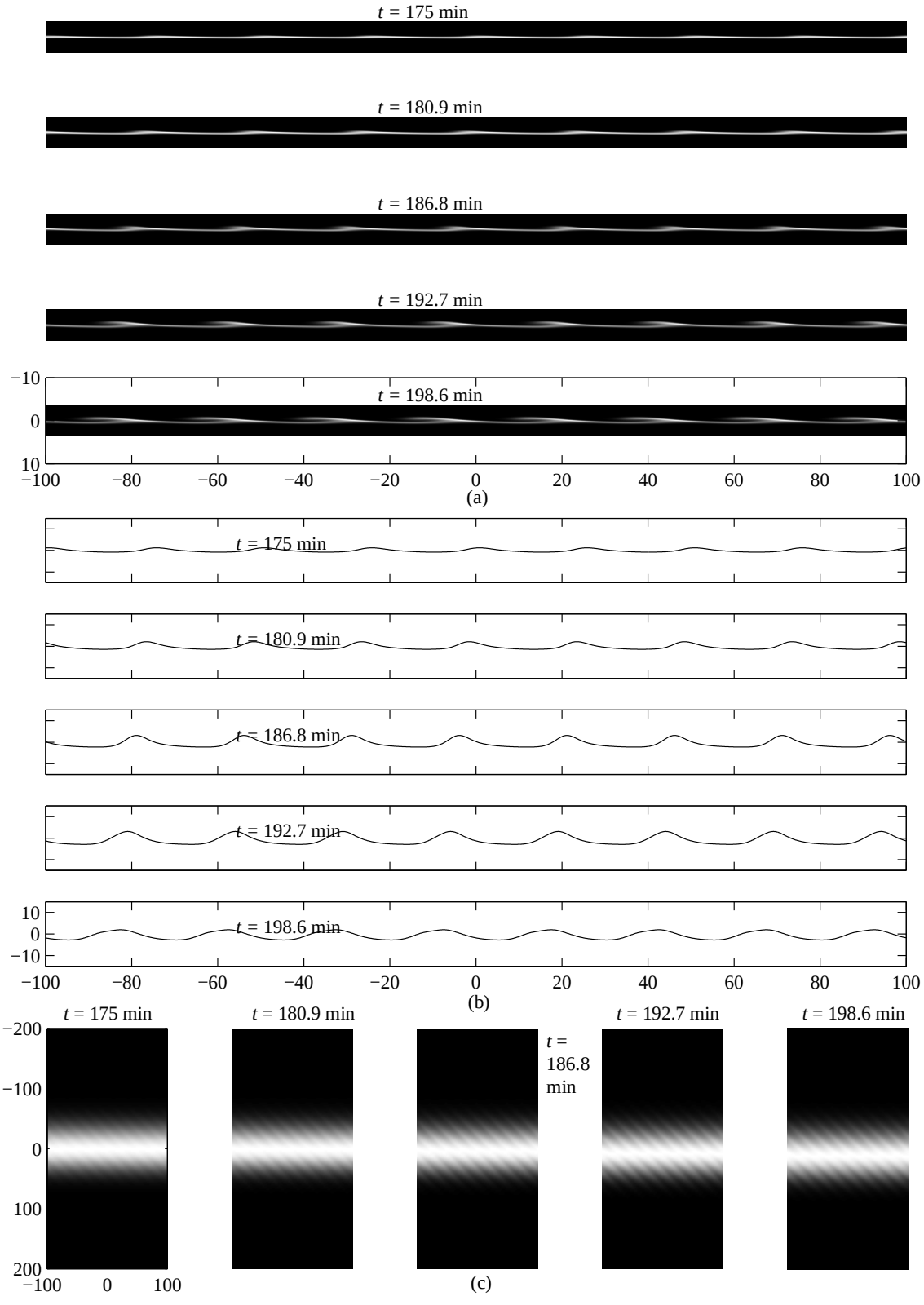

Fig. 5. Seed wavelength of 25 km with $\frac{\Sigma_H}{\Sigma_{PF}}$=1.8. **(a)** E_s layer, **(b)** electric field, and **(c)** F layer. The axes for all figures are described in Sect. 2.2, and summarized in Fig. 1.

together with the stronger electric fields, creates an increased F layer altitude modulation.

In Fig. 7 a possible interaction between large and small scale excitations of the E_s layer instability is illustrated. The simulation output for the 200 km wavelength excitation is taken as the initial state for the E_s and F layers. Representative of the effects of a lower-thermospheric gravity wave, we apply a $\pm$0.25 km amplitude, 25 km wavelength, sinusoidal altitude modulation to the E_s layer density profile at t=203.6 min, which is after the breaking wave (seen in Fig. 2) has subsided. The result, shown 12 min after the initial perturbation, is a 25-km-scale modulation of the polarization electric field, which exists over half the E_s layer extent (over 100 km). This result is reminiscent of observations (Saito et al., 2007) that show QP-echo-scale modulation of radar backscatter (assumed to be scatter from meter scale irregularities produced by a polarization electric field), within a larger-scale modulation envelope that matches the scale of the F-region-produced airglow.

3 Summary of conclusions and results

The conclusions and results of this work are summarized as follows:

1. In simplest form, the electric fields and spatial-scale of an excitation of the E_s layer at any stage of evolution scale directly with the spatial scale of the initial excitation. Specifically, when the initial excitation is rescaled as

$$n(t_0, x, y, z) \rightarrow \frac{1}{\sigma} n(t_0, x/\sigma, y/\sigma, z/\sigma) \tag{9}$$

(which rescales the wavelength as $\lambda \rightarrow \sigma\lambda$), then

$$\boldsymbol{E}(t, x, y, z) \rightarrow \sigma \boldsymbol{E}(t, x/\sigma, y/\sigma, z/\sigma) \text{ and}$$
$$n(t, x, y, z) \rightarrow \frac{1}{\sigma} n(t, x/\sigma, y/\sigma, z/\sigma)$$

for any later time t.

2. Under more realistic assumptions, simulations confirm that the electric fields and spatial-scale of the modes of the E_s layer instability increase with wavelength. The increase is significant, but not as rapid as by direct proportionality.

3. The increased electric fields, together with an increased interaction time, lead to a significant increase with wavelength of the F layer structuring associated with the E_s layer instability.

Items 1 through 3 suggest that the short wavelength ($\sim$20 km) modes of the E_s layer instability, which have the largest linear growth rate, may have little effect on the F layer. In fact, the effect shown in Fig. 5 is an exaggeration, since the largest growth rate modes were found by Cosgrove (2006b) to occur when the electric field produced by the E_s layer is partially decoupled from the F layer, due to short wavelength reduction in the efficiency of mapping along $\boldsymbol{B}$. This effect is not accounted for in the simulations.

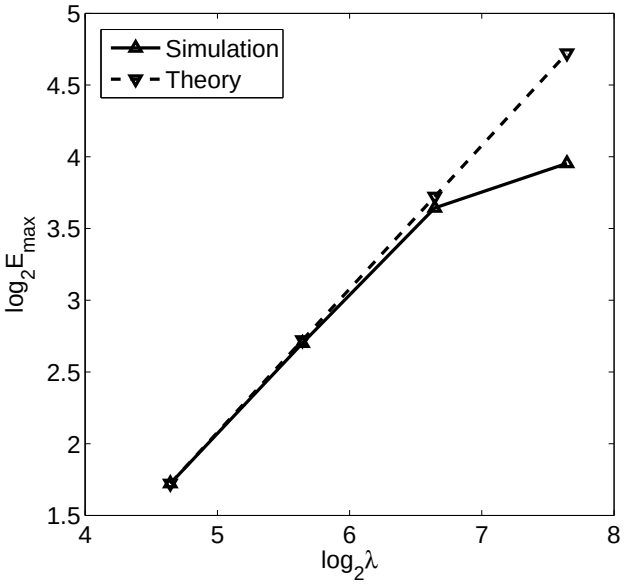

Fig. 6. $\log_2$-$\log_2$ plots of the peak electric field versus wavelength, as determined by the scaling rule of Sect. 2.1 (theory), and by the simulations presented in Figs. 2 through 5. The horizontal axis is $\log_2$ of wavelength in km, and the vertical axis is $\log_2$ of electric field in mV/m. The scaling rule is applied by setting the theoretical and simulated electric field equal at λ=25 km, and scaling to the longer wavelengths.

On the other hand, the longer the wavelength, the larger the polarization field that impacts the F layer, and the longer time it has to act. Therefore, we might expect that the longest wavelength that can be effectively initiated in the E_s layer, due to the operative seeding mechanism, and due to the finite size of the E_s layer, will be what is observed in the F layer.

An illustration of a possible interaction between large and small scale excitations is shown in Fig. 7, where it is seen that the large-scale excitation appears as an envelope for the smaller-scale excitation. This result is reminiscent of observations by Saito et al. (2007).

In summary, these results seem to be consistent with the observations of E_s and F layer frontal structures. The short wavelength modes are seen in the E_s layer, both because they have the largest growth rate, and because the long wavelength modes are difficult to observe. The latter is due both to the limited horizontal scale of E_s layer observation techniques, and to the fact that for long wavelength modes the evolution becomes strongly nonlinear before the altitude modulation becomes an appreciable fraction of the wavelength. The long

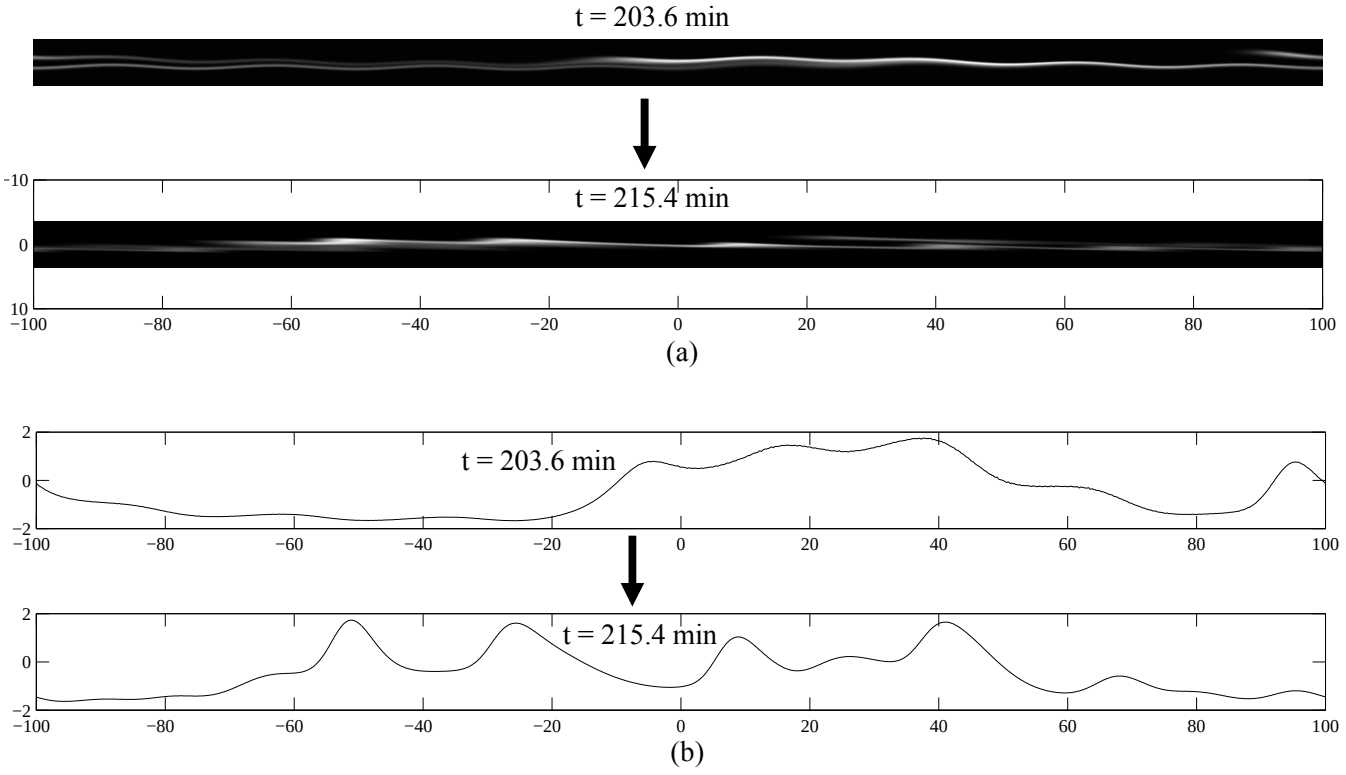

Fig. 7. The effects of a secondary, 25 km wavelength seeding of the E_s layer (e.g. by a gravity wave), after the 200 km seeding (by the F layer) has run its course. The times shown are measured from the initial 200 km seeding, except note that a ± 0.25 km amplitude, 25 km wavelength modulation has been imposed on the figures labeled t=203.6 min. Plasma density images are shown in panel **(a)**, and the corresponding electric fields are shown in panel **(b)**. The axes for all figures are described in Sect. 2.2, and summarized in Fig. 1.

wavelength modes are observed in the F layer because they are associated with larger polarization fields, and because the fields have a longer interaction time with the F layer plasma. The F layer evolution is less nonlinear, and produces altitude modulations that are an appreciable fraction of the wavelength, which can be observed by optical techniques with a large horizontal coverage.

In interpreting the simulation results, it is important to recognize that we have analyzed the electrodynamics of the coupled E_s and F layer system under the assumption that the external inputs are small, and act as mere "seeds". It is possible, in fact likely, that the external inputs are large. In such case the external inputs may dominate the dynamics. Hence, in the language of network theory, our result should be regarded as an analysis of the coupled E_s and F layer system response function. To obtain the response in an actual case scenario the drivers must be applied to the system response function. We make no attempt to do this in the present work. It is interesting that some characteristics of the observed phenomena match the characteristics of the system response function, but a complete analysis should consider application of the drivers.

Therefore, none of the assertions given above should be interpreted as a denial of the assertion made by Larsen et al. (2007) that neutral dynamics is the dominant driver behind the generation of E_s layer polarization electric fields, and QP echoes. We have merely supplied an analysis of the electrodynamical system function, as a step toward analysis of the driven system, that is, driven by waves or disturbances in the neutral atmosphere.

When $\Sigma_H / \Sigma_{PF} \lesssim 1$ the E_s layer is stable. The simulations of the system response function apply only in the case when the E_s layer is unstable. However, the theoretical development of Sect. 2.1 makes no assumption regarding stability. Hence, it is probable that even when the layer is stable longer wavelength drivers produce larger amplitude responses. In addition, it is clear that even when the E_s layer is stable it is easiest to excite waves aligned in the direction that is preferential for the instability.

Acknowledgements. This material is based upon work supported by the National Science Foundation under Grant No. 0436568. The author thanks Roland Tsunoda for valuable discussions.

Topical Editor M. Pinnock thanks S. Saito and another anonymous referee for their help in evaluating this paper.

References

Behnke, R.: *F* layer height bands in the nocturnal ionosphere over Arecibo, J. Geophys. Res., 84, 974–978, 1979.

Cathey, E. H.: Some midlatitude sporadic-*E* results from the Explorer 20 satellite, J. Geophys. Res., 74, 2240–2247, 1969.

Cosgrove, R. B. and Tsunoda, R. T.: A direction-dependent instability of sporadic-*E* layers in the nighttime midlatitude ionosphere, Geophys. Res. Lett., 29(18), 1864–1867, 2002.

Cosgrove, R. B. and Tsunoda, R. T.: Simulation of the nonlinear evolution of the sporadic-*E* layer instability in the nighttime midlatitude ionosphere, J. Geophys. Res., 108(A7), 1283, doi:10.1029/2002JA009728, 2003.

Cosgrove, R. B. and Tsunoda, R. T., Instability of the *E*-*F* coupled nighttime midlatitude ionosphere, J. Geophys. Res., 109, A04305, doi:10.1029/2003JA010243, 2004.

Cosgrove, R. B.: Generation of mesoscale F layer structure and electric fields by the combined Perkins and E_s layer instabilities, in simulations, Ann. Geophys., 25, 1579–1601, 2007a, http://www.ann-geophys.net/25/1579/2007/.

Cosgrove, R. B.: Wavelength dependence of the linear growth rate of the E_s layer instability, Ann. Geophys., 25, 1311–1322, 2007b, http://www.ann-geophys.net/25/1311/2007/.

Fukao, S., Kelley, M. C., Shirakawa, T., Takami, T., Tamamoto, M., Tsuda, T., and Kato, S.: Turbulent upwelling of the midlatitude ionosphere, 1, Observational results by the MU radar, J. Geophys. Res., 96, 3725–3746, 1991.

Fukao, S., Yamamoto, M., Tsunoda, R. T., Hayakawa, H., and Mukai, T.: The SEEK (Sporadic-*E* Experiment over Kyushu) Campaign, Geophys. Res. Lett., 25, 1761–1764, 1998.

Garcia, F. J., Kelley, M. C., and Makela, J. J.: Airglow observations of mesoscale low-velocity traveling ionospheric disturbances at midlatitudes, J. Geophys. Res., 105, 18 407–18 415, 2000.

Goodwin, G. L.: The dimensions of some horizontally moving E_s-region irregularities, Planet. Space. Sci., 14, p. 759, 1966.

Goodwin, G. L. and Summers, R. N.: E_s layer characteristics determined from spaced ionosondes, Planet Space Sci., 18, 1417–1432, 1970.

Johnson, F. S. (Ed.): The Satelite Environment Handbook, Stanford University Press, Stanford, CA, 1961.

Hysell, D. L., Larsen, M. F., and Zhou, Q. H.: Common volume coherent and incoherent scatter radar observations of mid-latitude sporadic E-layers and QP echoes, Ann. Geophys., 22, 3277–3290, 2004, http://www.ann-geophys.net/22/3277/2004/.

Kubota, M., Fukunishi, H., and Okana, S.: Characteristics of medium- and large-scale TIDs over Japan derived from OI 630-nm nightglow observation, Earth Planet. Space, 53, 741–751, 2001.

Larsen, M. F., Hysell, D. L., Zhou, Q. H., Smith, S. M., Friedman, J., and Bishop, R. L.: Imaging coherent scatter radar, incoherent scatter radar, and optical observations of quasiperiodic structures associated with sporadic *E* layers, J. Geophys. Res., 112, A06321, doi:10.1029/2006JA012051, 2007.

Otsuka, Y., Onoma, F., Shiokawa, K., Ogawa, T., Yamamoto, M., and Fukao, S.: Simultaneous observations of nighttime medium-scale traveling ionospheric disturbances and *E* region field-aligned irregularities at midlatitude, J. Geophys. Res., 112, A06317, doi:10.1029/2005JA011548, 2007.

Perkins, F.: Spread *F* and ionospheric currents, J. Geophys. Res., 78, 218–226, 1973.

Pfaff, R., Yamamoto, M., Marionni, P., Mori, H., and Fukao, S.: Electric field measurements above and within a sporadic-*E* layer, Geophys. Res. Lett., 25, 1769–1772, 1998.

Pfaff, R., Freudenreich, H., Yokoyama, T., Yamamoto, M., Fukao, S., Mori, H., Ohtsuka, S., and Iwagami, N.: Electric field measurements of DC and long wavelength structures associated with sporadic-E layers and QP radar echoes, Ann. Geophys., 23, 2319–2334, 2005, http://www.ann-geophys.net/23/2319/2005/.

Saito, A., Fukao, S., and Miyazaki, S.: High resolution mapping of TEC perturbations with the GSI GPS network over Japan, Geophys. Res. Lett., 25, 3079–3082, 1998.

Saito, A., Nishimura, M., Yamamoto, M., Fukao, S., Kubota, M., Shiokawa, K., Otsuka, Y., Tsugawa, T., Ogawa, T., Ishii, M., Sakanoi, T., and Miyazaki, S.: Traveling ionospheric disturbances detected in the FRONT campaign, Geophys. Res. Lett., 28(4), 689–692, 2001.

Saito, S., Yamamoto, M., Hashiguchi, H., Maegawa, A., and Saito, A.: Observational evidence of coupling between quasi-periodic echoes and medium scale traveling ionospheric disturbances, Ann. Geophys., 25, 2185–2194, 2007, http://www.ann-geophys.net/25/2185/2007/.

Shiokawa, K., Ihara, C., Otsuka, Y., and Ogawa, T.: Statistical study of nighttime medium-scale travelling ionospheric disturbance using midlatitude airglow images, J. Geophys. Res., 108(A1), 1052–1058, doi:1029/2002JA009491, 2003.

Tsugawa, T., Otsuka, Y., Coster, A. J., and Saito, A.: Medium-scale travelling ionospheric disturbances detected with dense and wide TEC maps over North America, Geophys. Res. Lett., 34, L22101, doi:10.1029/2007GL031663, 2007.

Tsunoda, R., Fukao, S., and Yamamoto, M.: On the origin of quasi-periodic radar backscatter from midlatitude sporadic *E*, Radio Sci., 29, 349–365, 1994.

Tsunoda, R. T. and Cosgrove, R. B.: Coupled electrodynamics in the nighttime midlatitude ionsphere, Geophys. Res. Lett., 28, 4171–4174, 2001.

Tsunoda, R. T., Cosgrove, R. B., and Ogawa, T.: Azimuth-dependent E_s layer instability: A missing link found, J. Geophys. Res., 109, A12303, doi:10.1029/2004JA010597, 2004.

Yamamoto, M., Fukao, S., Woodman, R. F., Ogawa, T., Tsuda, T., and Kato, S.: Midlatitude *E*-region field-aligned irregularities observed with the MU radar, J. Geophys. Res., 96(A9), 15 943–15 949, 1991.

Yamamoto, M., Komoda, N., Fukao, S., Tsunoda, R., Ogawa, T., and Tsuda, T.: Spatial structure of the *E* region field-aligned irregularities revealed by the MU radar, Radio Sci., 29(1), 337–347, 1994.

Yamamoto, M., Kumura, F., Fukao, S., Tsunoda, R. T., Igarashi, K., and Ogawa, T.: Preliminary results from joint measurements of E-region field-aligned irregularities using the MU radar and the frequency-agile radar, J. Atmos. Solar Terr. Phys., 59, 1655–1663, 1997.

Yamamoto, M., Fukao, S., Tsunoda, R. T., Pfaff, R., and Hayakawa, H.: SEEK-2 (sporadic-E experiment over Kyushu 2)-project outline, and significance, Ann. Geophys., 23, 2319–2334, 2005, http://www.ann-geophys.net/23/2319/2005/.